

Experimental and Numerical Study of the Effect of Varying Sinusoidal Bumps Height at the Leading Edge of the NASA LS (1)-0413 Airfoil at Low Reynolds Number


 Open
Access

Bashir Isyaku Kunya^{1,*}, Clement O. Folayan², Gyang Yakubu Pam², Fatai Olukayode Anafi², Nura Muaz Muhammad¹

¹ Department of Mechanical Engineering, Kano University of Science and Technology, Wudil, Nigeria

² Department of Mechanical Engineering, Ahmadu Bello University, Zaria, Nigeria

ARTICLE INFO

Article history:

Received 10 October 2018

Received in revised form 2 January 2019

Accepted 20 March 2019

Available online 23 March 2019

Keywords:

Angle of attack, lift coefficient, drag coefficient, bumps height, Reynolds number.

ABSTRACT

This research work is about numerical simulation and experimental study of the effect of varying sinusoidal bumps (or tubercles) height at the leading edge of the airfoil on efficiency using NASA LS (1)-0413 cross-section profiles. Spalart Allmaras turbulence model was used for numerical solutions. The parameters investigated include, lift, and drag, the angle of attack and bumps height at very low Reynolds number of 4.9×10^4 . The results show that bumps on the blade leading edge have an advantage at post-stall angles of attack on the performance and varies with bumps height.

Copyright © 2019 PENERBIT AKADEMIA BARU - All rights reserved

1. Introduction

An airfoil is a streamline body, i.e., it has a rounded leading edge, elongated and has a gradual curvature in the flow direction. The airfoil sections employed for airplane wings, propellers, wind turbine, etc. are of such a geometrical configuration to produce high lifts and low drag values. The lift on an airfoil is primarily the result of its angle of attack and shape. When oriented at a suitable angle, the airfoil deflects the oncoming air, resulting in a force on the airfoil in the direction opposite to the deflection [1]. Airfoils mostly look quite different from one another and designers have not settled on the best one because the flow conditions and design goals change from one application to the next.

The answer for improving the performance of airfoil may lie with the flippers of humpback whales. The humpback whale (*Megaptera novaeangliae*) is a species of the largest group of baleen whale. The humpback has a distinct body shape, with long pectoral flippers (fins) and a knobby head. It is known for breaching, tail-lobbing and pectoral fin slapping as the common surface

* Corresponding author.

E-mail address: kunjabashir@yahoo.com (Bashir Isyaku Kunya)

behavior. The flippers have a series of sinusoidal-shaped bumps called tubercles on their leading edge [2]. Some researchers employed this technique in their analysis [3-5].

Introduction of tubercles (bumps) on airfoil leading edge can make an impact on the airfoil performance the same way it does for the humpback whale. Some computational and experimental research works have been conducted to study the impact of bumps on airfoil performance [6-9]. The survey of the previous studies revealed that the leading-edge tubercles allow the operation of the airfoil at a higher angle of attack before stall (separation) would occur, thus, improving its performance. Hansen *et al.*, [10] ran an experimental test to compare the performance of two machined and anodized aluminum NASA airfoils with sinusoidal leading-edge protuberances, to conventional foils of the same dimensions but with smooth leading edges. Their wind tunnel tests results show that the tubercle leading edge was more beneficial for the NASA 65-021 foil than for the NASA 0021 foil and that both tubercle foils showed increased maximum lift coefficient and a larger stall angle than the conventional foil. Measurements of lift and drag were performed versus angle of attack over a range of Reynolds numbers from 1.2×10^5 to 2.74×10^5 . They also studied the influence of tubercle bump height (from 3% to 11% of chord), and sinusoidal wavelength (from 11% to 86% of chord). They found that increasing wavelength improved stall characteristics, but also slightly reduced the maximum lift coefficient. They confirmed prior results that at a low angle of attack there is little difference, in lift or drag performance between otherwise identical conventional, smooth leading-edge foils, and those with tubercles. At a higher angle of attack, the benefits decrease with increased bump height beyond some yet to be determined optimum bump height value that seems to depend upon both Reynolds number and bump wavelength.

Menter *et al.*, [11] conducted numerical analysis with four eddy viscosity turbulence models under adverse pressure gradients condition and compared with experimental data. They reported severe retardation of the boundary layer in some cases and separation in one of the cases. Ahmed *et al.*, [12] carried out a numerical simulation of the effect of tubercles on the flow characteristics around NASA 0012 airfoil. The angle of attack was varied from 0° to 25°, and the values of Reynolds number ranged between 65,000 and 1,000,000. The standard k- ϵ model was used as the turbulence modeling technique. It was found that tubercles delayed stall at a higher angle of attack. For both the regular and tubercle airfoils the maximum value of lift coefficient and the angle at which stall occurs increases with Reynolds number. The values of the drag coefficient of tubercle airfoil are greater than those of regular airfoil.

Investigation of the leading-edge protuberances on a thick airfoil (S809) was also carried out by Majid, *et al.*, [13]. The airfoil was analyzed by computational fluid dynamics (CFD) method in 106 Reynolds number. The results revealed that, at low angles of attack before the stall region, lift coefficient decreases slightly rather than the baseline model. However, the modified airfoil has a smooth stall trend while the baseline airfoil lift coefficient decreases sharply due to the separation which occurred on a suction side.

Zhao *et al.*, [14] carried out numerical analysis of the flow characteristics behind the effects of leading-edge protuberances on NACA 634-021 airfoil performances at low Reynolds number. Their investigations were focused on the stall and post-stall regions, respectively. It was found that the tubercle airfoil could provide more aerodynamic lift than the smooth one within the post-stall region and the stalled process was rather gentle. An interesting 'biperiodic' phenomenon within stall region, i.e. converged and diverged vortical flow in adjacent trough sections of tubercles, was created with the complicated evolution of the generated streamwise counter-rotating vortex pairs, resulting in the degraded aerodynamic characteristics. For the post-stall cases, the impaired flow detachment around both peak and trough sections of tubercles were responsible for the improved airfoil performance.

Recently, computation of lift and drag of ONERA M6 wing have been conducted by Munshi *et al.*, [15] on winglet modification that reduces tip vortex. Flow features were examined at different cant angles of winglets (30°, 60°, and 75°) at different angles of attack from 3° to 6°. It is observed that wings with winglets produce higher CL/CD ratio than the normal aircraft wing without winglets up to a certain degree of angle of attack and by further increasing to a higher angle of attack its performance getting diminished.

It's the believe of the authors that there is need to carry out research to know the effect of bumps height variation and to identify the optimum height at airfoil leading edge for aerodynamics applications at low Reynolds number (4.9×10^4), based on the available literature, it was the first time a research on experimental and numerical study on the effect of varying sinusoidal bumps height at the leading edge of the NASA LS (1)-0413 airfoil at very low Reynolds Number was conducted.

2. Methodology

This study is limited to the computational and experimental study of the effect of sinusoidal bumps height variation (and to identify the optimum height) at the leading edge of the airfoil (NASA LS (1)-0413 cross-section profiles) at very low Reynolds number. The study parameters include lift and drag, and angle of attack. Spalart Allmaras turbulence model was used for numerical solutions.

The airfoil profile selected is NASA LS (1) - 0413. The LS (1) represent low-speed first series, the first two digits after the dash represent the design lift coefficient (0.4) and the last two digits represent the maximum thickness to chord ratio (13%). This airfoil is shown best performance during wind tunnel test at 4×10^6 Reynolds number than another LS (1) airfoils (LS (1) – 0409, 0417, 0421) tested. It had greater maximum lift coefficient of 1.9 and lift to drag ratio of about 100. The maximum Lift Coefficients for this thickness family were substantially greater than the older NACA airfoils of comparable thickness ratios [16].

For this study, bumps with sinusoidal shape, 6% chord length bump height (as approximately there on the natural whale pectoral fins from the study of Howle *et al.*, [17]; and inter-bumps distance of 22% span was first designed for the selected NASA airfoil section using CAD software (Gambit). Bumps heights, 2% (0.02C), 4% (0.04C), 6% (0.06C), 8% (0.08C), and 10% (0.10C) chord length with inter-bumps distances of 22% (0.22S) span were studied as well.

The airfoil models and the C-grid domain were created in Gambit modeling software. Table 1 shows the geometrical details of the models and Figure 1 shows the illustrations of the models.

Table 1
Geometrical details of airfoil models

Airfoil model	Bumps height
CLEM-00	conventional model
BLEM-2C-22(5)S	2% of chord
BLEM-4C-22(5)S	4% of chord
BLEM-6C-22(5)S	6% of chord
BLEM-8C-22(5)S	8% of chord
BLEM-10C-22(5)S	10% of chord

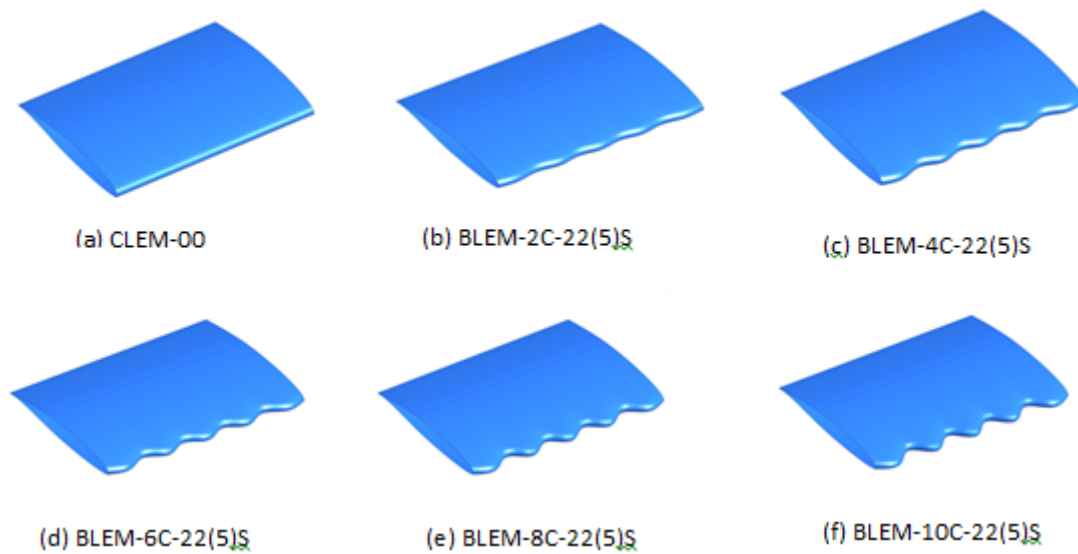


Fig. 1. Airfoil models with an inter-bumps distance of 22% of span

Four volumes were created within a C-grid computational domain and meshed (Figure 2).

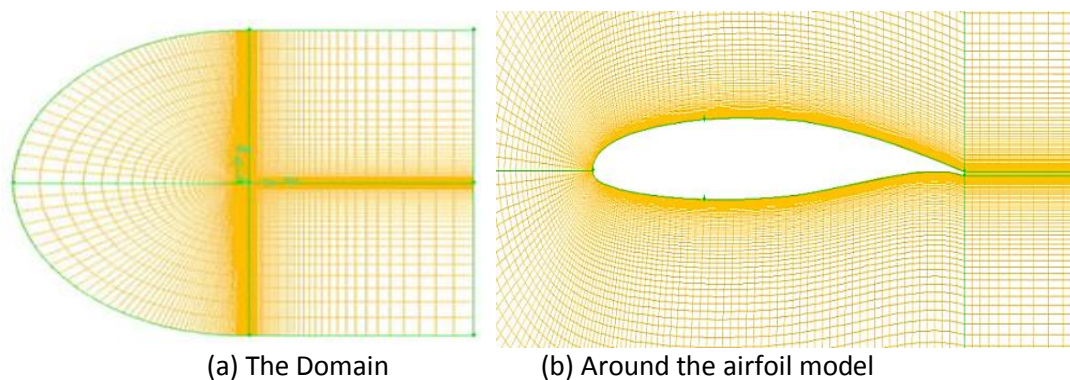


Fig. 2. The mesh

The mesh file was exported into fluent solver as an msh file and set-up the simulation. The pressure-based solver was used to perform the simulations in fluent. The semi-implicit method for pressure-linked equations (SIMPLE) scheme (the default scheme, and very robust) was used to resolve the pressure-velocity coupling. Pressure-velocity coupling refers to the numerical algorithm which uses a combination of continuity and momentum equations to derive an equation for pressure (or pressure correction) when using the pressure-based solver. As suggested by the solver [18], the first-order upwind scheme was implemented and then switched to second-order upwind scheme for discretizing the convective terms of the momentum equation and second-order was also used as the pressure interpolation scheme (finding the pressure at the cell-faces). Second-order pressure interpolation scheme reconstructs the face pressure in the manner used for second-order accurate convection terms. This scheme may provide an improvement in the accuracy over the standard and linear schemes. Default under-relaxation factors (used to increase the stability of the calculation) provided in the solver was used.

The experimental method involved testing the models (constructed with a three-dimensional printer) in the wind tunnel. The experiment was performed in wind tunnel AF100 SUBSONIC OPEN CIRCUIT (Figure 3) with the following specifications: 0.305m x 0.305m test section and 0 – 36m/s nominal air velocity.

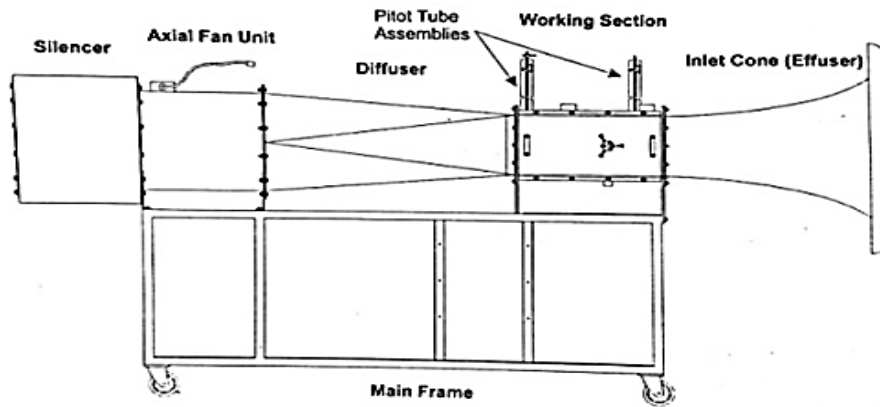


Fig. 3. AF100 Subsonic Open Circuit Wind Tunnel Layout

The experimental models were manufactured using a direct digital manufacturing (3D printing) process. The models were manufactured with a U-Print SE Plus printer (Figure 4). A computer model was generated and imported (as stl format) into the 3D printer software and is automatically 'sliced' into multiple layers. The slices were then built by the printer by depositing plastic material particles one layer at a time until the model was fully formed.



Fig. 4. The U-Print SE Plus printer producing the airfoil model

The conventional airfoil model, models with 0.02C, 0.04C, 0.06C, and 0.08C bumps height and 22% inter- bumps distance were manufactured by the printers using a plastic material known as ABS (Acrylonitrile Butadiene Styrene) shown in (Figure 5). Models sizes (span and chord length) are the same as the computer models used for the simulation.



Fig. 5. Physical Aerofoil Models

The experiment was conducted using AF100 subsonic open circuit wind tunnel machine as mentioned earlier. A Single Component Balance (AFA2) that came with the machine was used for the measurement of lift and drag forces. The procedure is as follows:

- I. AFA2 Component Balance was placed on to the back plate (mounted at one of the sides of the working section) using the smaller thumbscrews supplied. Figure 6 shows the AFA2 component balance mounted at one of the sides of the wind tunnel test section.

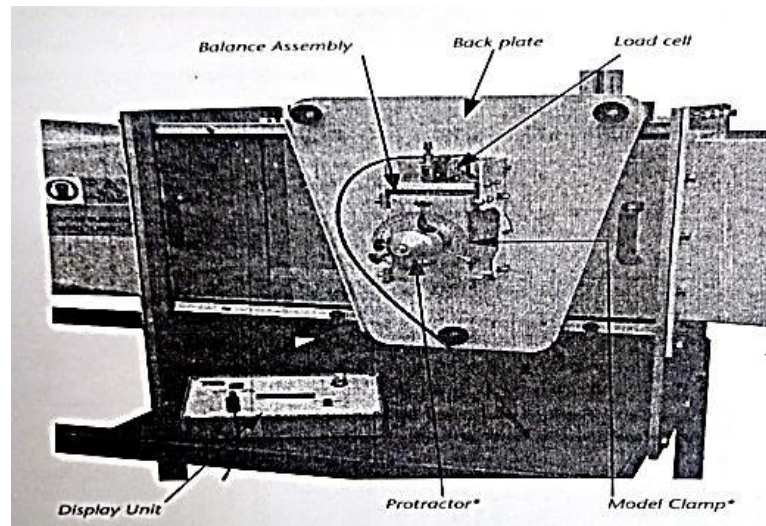


Fig. 6. AFA2 Component Balance Assemblies [19]

- II. For drag measurement, the assembly was fitted so that the load cell is to the right. For lift measurement, the assembly was rotated and fixed so that the load cell is to the top; you will hear and feel a ball spring mechanism lock in to place when the assembly is in position.
- III. The clear window from the opposite side of the working section was removed and mounted the airfoil model into the working section and slides its support shaft through the hole in the middle of AFA2 Balance Assembly (Figure 7).

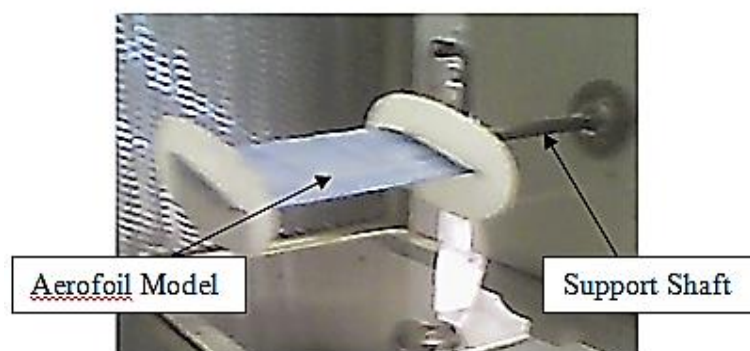


Fig. 7. One of the Physical Model inside Wind Tunnel Test Section

- IV. The airfoil model was set to zero angles and flew upside down, and tighten the three thumbscrews on the Balance Assembly to clamp the model
- V. Fitted the protractor to the model shaft and set it to zero degrees. Tighten the protractor clamp screws.
- VI. The clear window to the opposite side of the working section was replaced

- VII. Connected the display unit and switched on the electric supply to the control and instrumentation unit of the wind tunnel machine.
- VIII. The system was switched on and left the display unit to stabilize for five (5) minutes.
- IX. The zero buttons were pressed and held for at least four seconds to re-zero the force reading.
- X. The experiment was started by turning the wind tunnel to the desired airspeed (7.1 m/s in this study) by calculating the corresponding dynamic pressure (ΔP) and thus set-up the wind tunnel manometer reading in mmH₂O (Eq. (1)).

$$\Delta P = \frac{V^2 \rho_a}{2g} \quad (1)$$

Where, V is the velocity of air, ρ_a is the air density, and g is acceleration due to gravity.

- XI. Results were Read and recorded.

2.1. Governing Equations

Fluid dynamics is the study of fluid motion that involves forces of action and reaction, i.e. forces which cause acceleration and forces which resist acceleration. The equations governing the fluid motion are mass and momentum equations presented as flows: [20]

Continuity equation

$$\frac{\partial \rho}{\partial t} + \nabla \cdot (\rho V) = 0 \quad (2)$$

Momentum equation

$$\rho \frac{\partial V}{\partial t} + V \cdot \nabla (\rho V) = \nabla \cdot \tau_{ij} - \nabla P + \rho F \quad (3)$$

Where ∇ is $\left(\frac{\partial}{\partial x} + \frac{\partial}{\partial y} + \frac{\partial}{\partial z}\right)$, ρ is the fluid density, V is the fluid velocity vector, τ_{ij} is the viscous stress tensor, P is pressure, and F is the body forces.

Presence of each term and their combination determines the appropriate solution algorithm and the numerical procedure.

The Reynolds average Navier-Stokes (RANS) Eq. (4-5) are primarily used to describe turbulent flows.

$$\nabla \cdot \bar{V} = 0 \quad (4)$$

$$\frac{\partial \bar{V}}{\partial t} + \bar{V} \cdot \nabla \cdot \bar{V} = \frac{\mu}{\rho} \nabla^2 \bar{V} - \frac{1}{\rho} \nabla \cdot \bar{P} + \bar{F} - \overline{\nabla \cdot V^2} \quad (5)$$

The non-linear Reynolds stress term $\left(\overline{\nabla \cdot V^2}\right)$ requires additional modeling to close the RANS equation for solving and has led to the creation of many different turbulence models.

Spalart Allmaras is one-equation, low-cost RANS model solving a transport equation for a modified eddy viscosity, $\tilde{\nu}$.

$$\frac{D\tilde{v}}{Dt} = G_V \left\{ \frac{\partial}{\partial y} \left[(\mu + \rho\tilde{v}) \frac{\partial\tilde{v}}{\partial y} \right] + C_{b2}\rho \left(\frac{\partial\tilde{v}}{\partial y} \right)^2 \right\} - Y_v + S_{\tilde{v}} \quad (6)$$

The eddy viscosity is obtained from

$$\mu_t = \rho\tilde{v}f_{vI} \quad (7)$$

$$f_{vI} = \frac{(\tilde{v}/\nu)^3}{(\tilde{v}/\nu)^3 + C_{vI}^3} \quad (8)$$

The variation of \tilde{v} very near the wall is easier to resolve than k and ϵ . The model is designed specifically for aerodynamic or turbo machinery applications with mild separation such as supersonic/transonic flows over airfoils, boundary layer flow, etc. Option to include strain rate in k production term improves predictions of vortical flows.

2.2. Grid Independent Study

Grid-independent study was carried out by generating an initial grid of low resolution and then using the same meshing scheme to generate grids of higher resolutions. Many grids were generated and used to run the simulation using identical solver settings after which the solutions of lift and drag coefficients were then compared. All simulations for the grid study were conducted using the NASA LS (1) – 0413 conventional airfoils at an angle of attack of 5 degrees and velocity of 6m/s. The results are tabulated (Table 2).

As seen from Table 2 the lift coefficient changes from the first grid to the second, but insignificantly changed after the second grid and it maintained a lift coefficient of around 0.84 from the fourth grid. Similarly, the drag coefficient reduces from grid one to grid two but maintained a close value after grid three with an average drag coefficient of 0.032. Due to this, the Fourth grid with a resolution of 1655000 cells is chosen as the basis for all the grids in this work.

Table 2
Grid convergence study

Grid	Resolution (Cells)	Lift Coefficient	Drag Coefficient
1	224000	0.79693	0.033915
2	980000	0.82985	0.031595
3	1385000	0.83498	0.031998
4	1655000	0.83984	0.031995
5	1925000	0.84095	0.031742
6	2195000	0.84129	0.032082

2.3. Boundary Conditions

To solve the governing fluid dynamic equations so as to obtain the pressure and velocity fields within the flow domain to calculate for lift and drag forces, boundary conditions were specified.

The inlet and outlet fluid velocities were specified as the free air stream velocity (V_0). The fluid velocity differential through the symmetry boundaries (i.e. the other two sides of the computational domain) are zero.

$$\nabla \cdot V = 0 \quad (9)$$

The fluid velocity at the airfoil wall was specified as zero.

2.4. Aerodynamic Forces

A fluid flowing past an airfoil causes the fluid to divert from its original path, such change in direction lead to changes in the pressure and the velocity of the fluid. The fluid experiences resistance forces (frictional forces) as it flows due to its viscosity. This force and the force arising from the pressure over the surface of the body is collectively the resultant force exerted by the fluid on the body, known as the aerodynamic force. The aerodynamic force is customarily resolved into two orthogonal components that are directionally referenced to the free stream velocity (V) [21]:

- I. Drag-component (D) parallel to the direction of the relative motion
- II. Lift- component (L) perpendicular to the direction of the relative motion

Figure 8 shows the direction of these forces exerted by the fluid on the airfoil.

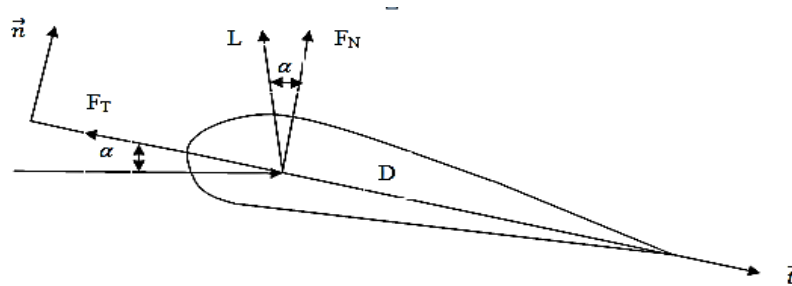


Fig. 8. Airfoil Aerodynamic forces

Where D is drag force per unit length, L is lift force per unit length, F_N is total normal force per unit length, F_T is total tangential force per unit length, \vec{t} is unit vector aligned to the chord, and \vec{n} is a unit vector perpendicular to the chord. Also, lift and drag coefficients are respectively given as [21]:

$$C_L = \frac{L}{\frac{1}{2} \rho U_0^2 c} \quad (10)$$

$$C_D = \frac{D}{\frac{1}{2} \rho U_0^2 c} \quad (11)$$

3. Results

The 'lift' and 'drag' Coefficients obtained are presented in graphs. The results of the simulation are also viewed by generating contour plots of the domain using commercial Fluent post-processing capabilities.

3.1. Numerical Results and Discussion

The graphs of lift and drag coefficients are shown respectively in the Figure 9 and 10 for CLEM-00 and bumpy airfoils (bumps height: 2%, 4%, 6%, 8%, and 10% chord length; inter-bumps distances: 22% span) at 7.1m/s, and at various angles of attack (-10° to 25°).

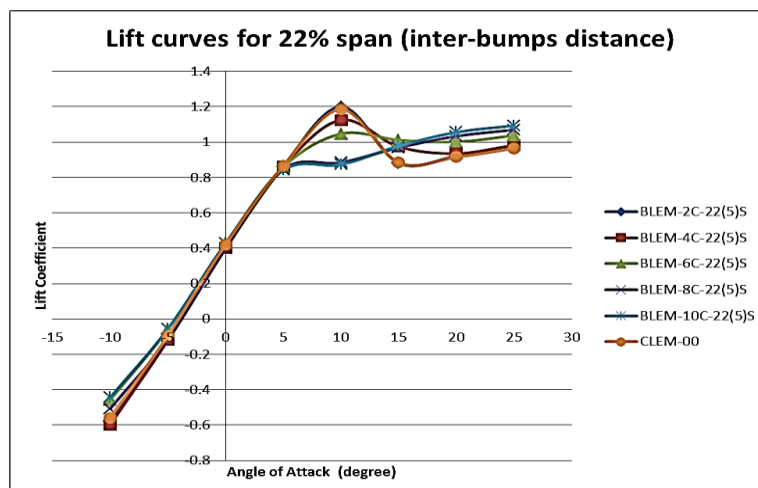


Fig. 9. Variation of Lift coefficient with angle of attack by varying bumps height

For all airfoils regardless of bump height, the lift curve from -10 degree to 5 degrees is linear. They have different lift coefficients at -10 degrees and slowly converging to a point at around 5 degrees, after which stall effects begin and the airfoils start to diverge. At around 10 degrees a pattern is observed whereby the CLEM-00 and the BLEM-2C-22(5)S have the highest lift coefficient followed by BLEM-4C-22(5)S and then BLEM-6C-22(5) S. Also, at 10 degrees, the BLEM-8C-22(5)S and BLEM-10C-22(5)S have approximately the same and lower lift coefficients. After 15 degrees the effects of the bumps is clearly seen for higher angles of attack. BLEM-6C-22(5)S and BLEM-10C-22(5)S show closer lift values from 15 degrees to 20 degrees and both are having higher lift values than the other airfoils. The simulation shows that the smaller the bump size the lower the lift coefficient curve within the range, 20° to 25° angle of attack. The BLEM-2C-22(5)S has the lowest lift coefficient followed by the BLEM-4C-22(5)S, the BLEM-8C-22(5)S comes in next and finally, we have the BLEM-10C-22(5)S with the highest lift coefficient curve.

From the drag graph (Figure 10), at -10 the BLEM-10C-22(5)S has the highest drag coefficient while the rest of the airfoils show smaller differences of drag coefficients. From -10 to 0 degree each airfoil drag value reduces to zero at zero angles of attack. And From zero to five degree, all airfoils have almost the same drag coefficients. After 5 degree a pattern is observed whereby the graphs for airfoils with higher bump heights (BLEM-6C-22(5)S, BLEM-8C-22(5)S and BLEM-2C-22(5)S) follow nearly a straight line, while that for BLEM-2C-22(5)S, BLEM-4C-22(5)S, and CLEM-00 follow a nonlinear path. All airfoils converge at 15 degrees and follow a linear path and aligned up to 25 degrees.

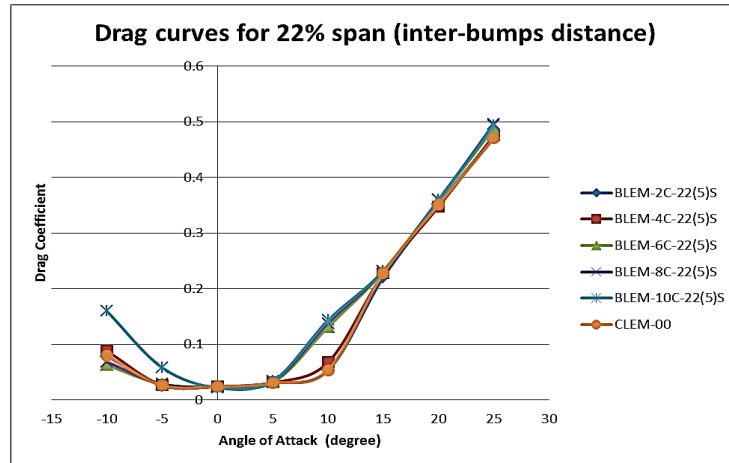


Fig. 10. Variation of Drag coefficient with angle of attack by varying bumps height

3.2. Pressure and Velocity Contours

Generally, a high pressure region exists below the model, and the low-pressure region is on top of it. Due to the pressure difference, the flow from the bottom surface to the top surface at the trailing edge creates a low-pressure region. This low-pressure region is much lower than the pressure on the top surface, which creates a favourable pressure gradient in the front part but an adverse pressure gradient in the rear part, as shown below. This adverse pressure gradient slows down the velocities inside the boundary layer which causes the recirculation region close to the top surface of the airfoil. This recirculation region continues to grow upstream as more air is accelerated from bottom to top surface of the airfoil. Figure 11 shows the contours of pressure.

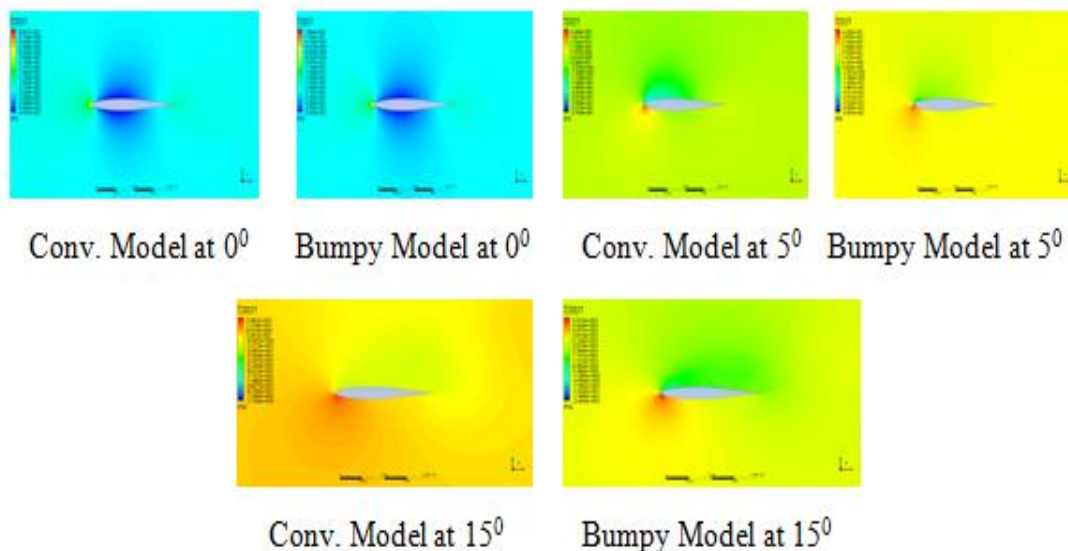


Fig. 11. Pressure Contours

Flow over the airfoil boundaries is intact from the angle of 00 to 50, there is no flow separation and the lift curves are aligned for both conventional and bumpy airfoils. At 5°, flow separation starts for all the airfoils and continue at higher angles, the effects of drag becomes dominant and the airfoil enters stall conditions. Figure 12 show the velocity contours.

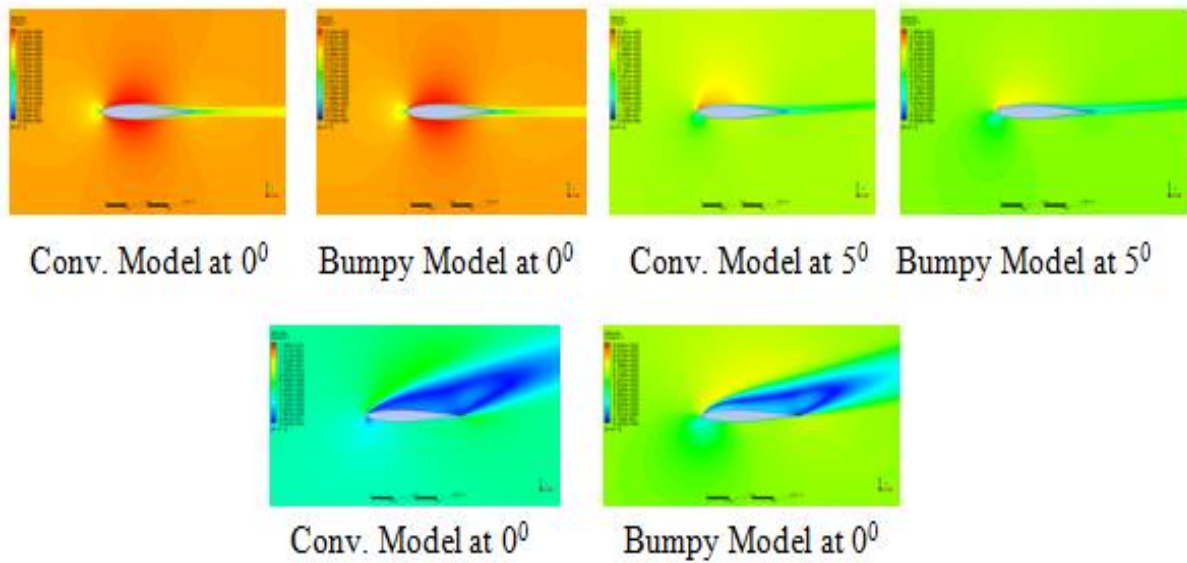


Fig. 12. Velocity Contours

Contours of velocity at a 15° angle of attack for the conventional and bumpy airfoils are compared. Flow separation is delayed for the airfoils with bumps. A study by Howle *et al.*, [17] revealed that tubercles (bumps) at the airfoil leading edge act as passive-flow control devices that improve performance and increase in effective span. They produced stream-wise vortices that carried higher momentum flow in the boundary layer, which kept the flow attached to the surface of the airfoil and, in turn, delayed separation, and thus enables a higher lift coefficient during post stall.

3.3. Experimental Results and Discussion

The graphs of lift and drag coefficients are shown respectively by the Figure 13 and 14 for CLEM-00, BLEM-2C-22(5)S, BLEM-4C-22(5)S, BLEM-6C-22(5)S, and BLEM-8C-22(5)S at 7.1m/s, and at various angles of attack (-10° to 25°).

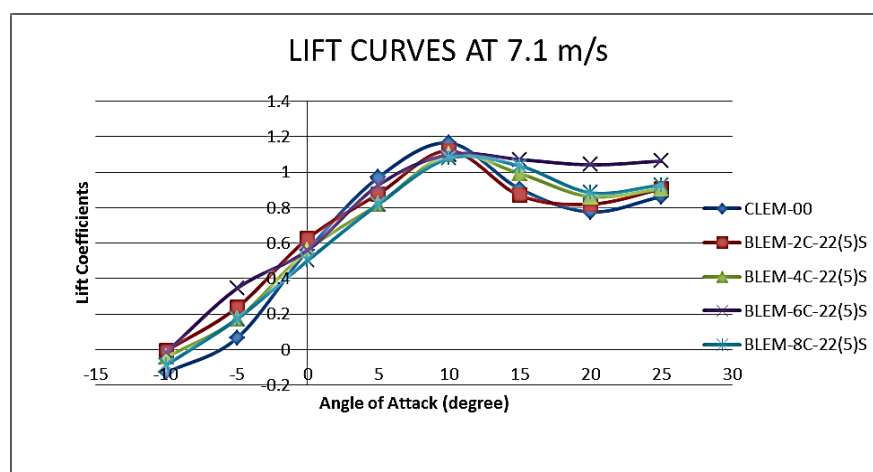


Fig. 13. Variation of Lift coefficients with angles of attack by varying bumps height

For all the models regardless of bump height, the lift curve from -10 degree to angle closer to 10 degree is approximately linear. At around 10 degrees a pattern is observed whereby the CLEM-00 and the BLEM-2C-22(5)S have the highest lift coefficient. Also, at 10 degrees, BLEM-4C-22(5)S, BLEM-6C-22(5)S, and BLEM-8C-22(5)S have a lower maximum lift coefficient. After around 10 degrees the effects of the bumps has started and is clearly seen for higher angles of attack most especially for BLEM-6C-22(5)S then followed by BLEM-4C-22(5)S and BLEM-8C-22(5) S. The experiment shows that the smaller the bump size the lower the lift coefficient curve within the region of 15⁰ to 25⁰.

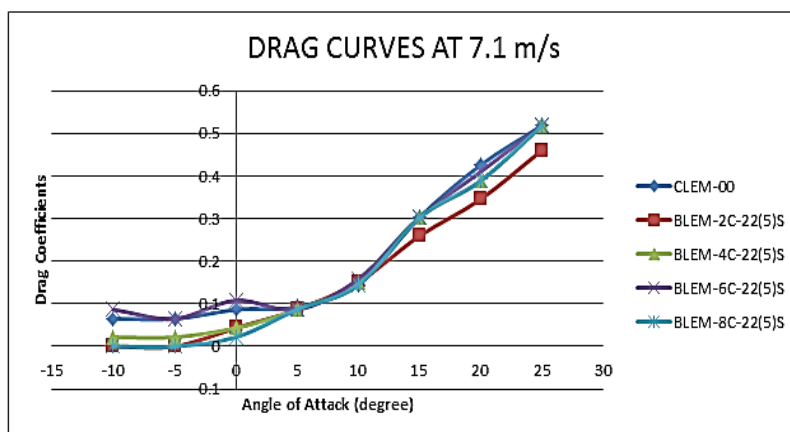


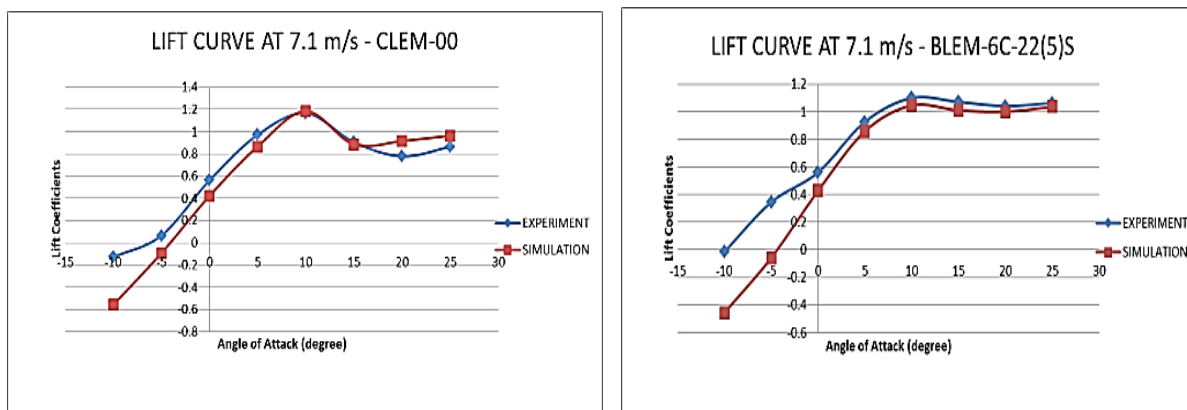
Fig. 14. Variation of Drag coefficients with angles of attack by varying bumps height

From -10 to 5-degree CLEM-00 and BLEM-6C-22(5)S have the highest drag coefficients while the rest of the airfoils have an almost similar range of drag coefficient at these angles. From 10 degree up to 25 degrees, all the models have almost the same drag coefficients except for BLEM-2C-22(5)S with lower drag values from 15 to 25 degrees.

3.4. Comparison of the Simulation Results with Experimental Results

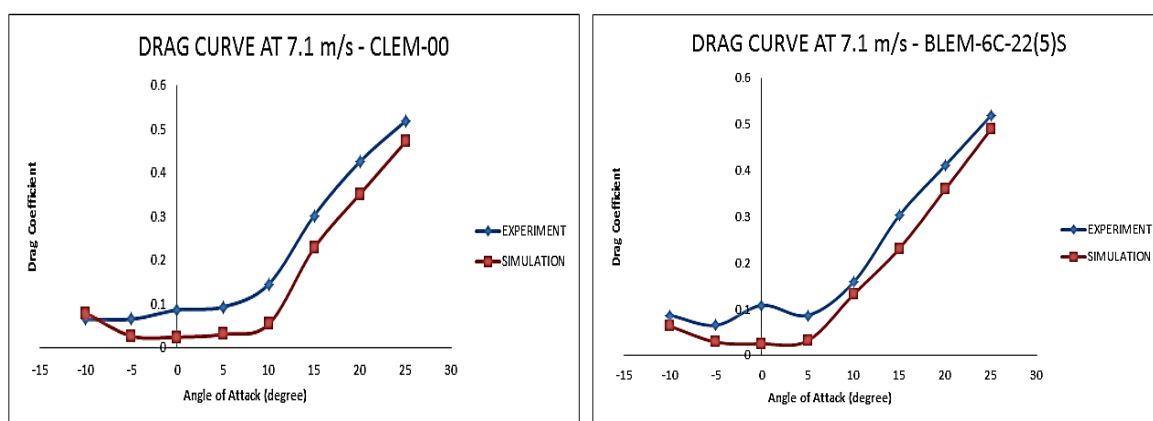
Simulation results were compared with the experimental results to see their level of agreement; the lift and drag results for the CLEM-00 and the BLEM-6C-22(5)S were compared and discussed in the following sub-headings.

The comparison of the lift coefficients as a function of the angle of attack is shown in Figure 15. The simulation results of both models are in good agreement with experimental values. The lift values increase in the linear rate until around stall angle which is the 10-degree angle of attack. Closer agreements occur for both models except that the simulation under predict experiment at negative angles.



(a) CLEM-00 (b) BLEM-6C-22(5)S
Fig. 15. Comparison of Experimental and Simulation Lift Value at 7.1m/s

Generally, the nature of the simulation and the experimental graphs of the drag coefficients are similar; the rate of variation of drag values with the angle of attack is approximately the same, thus closer agreements. However, the simulation under-predicts drags values for all positive angles of attack. See Figure 16.



(a) CLEM-00 (b) BLEM-6C-22(5)S
Fig. 16. Comparison of Experimental and Simulation Drag Value at 7.1m/s

As explained earlier the simulation results show good agreement with the experimental one because the nature of the graphs seems very similar as the rate at which the lift and drag values vary with angle of attack is approximately the same. The absolute values of the lift coefficients show little differences between the numerical and experimental results; the average percentage error is 6% for CLEM-00 and 4.3% for BLEM-6C-22(5) S. The variations might be due to more difficulty and uncertainty in setting up the manometer reading of the wind tunnel to give the desired air velocity, and generally, uncertainty with the manual setting of the airfoil angle of attack in the wind tunnel. Therefore, the result of the experiment has validated the numerical result.

4. Conclusions

A numerical study on the effect of varying sinusoidal bumps height at the leading edge of the NASA LS (1)-0413 airfoil was conducted and validated with experiment at very low Reynolds Number of 490000. From the results, the following important issues were concluded:

- a) The bumpy airfoils showed increased maximum lift coefficient and a larger stall angle than the conventional airfoil due to the production of stream-wise vortices along the leading edge of the bumps. These vortices carried higher momentum flow in the boundary layer, which kept the flow attached to the surface of the airfoil and, in turn, delayed separation, and thus enables a higher lift coefficient during post stall.
- b) The conventional airfoil model has the highest lift value from around 5° up to stall where it has maximum lift coefficient. However, the bumpy airfoil models have greater lift coefficients during post stall after around 15° angles of attack.
- c) Generally, the higher the bump height the higher the lift values and all the airfoils show almost the same drag coefficients from around 15° to above angle of attack.
- d) Effect of varying bumps height on drag is that, between angles -10° and -5° , the same thing between 5° and 15° , the BLEM-2C-22(5)S, BLEM-4C-22(5)S, and conventional airfoils have closer drag coefficients values but lower than that of BLEM-6C-22(5)S, BLEM-8C-22(5)S and BLEM-10C-22(5)S airfoils. The last group also show closer drag coefficients values at the stated angles range.
- e) Angles of attack between 15° and 25° were good performing angles for bumpy airfoil model because flow separation is relatively minimal than that of the conventional model. Bumps height of 6% chord length was generally better in airfoil performance.

Acknowledgment:

Experiments were conducted using a wind tunnel facility in the Department of mechanical engineering, Ahmadu Bello University, Zaria free of charge.

References

- [1] J. Douglas, J. Gasiorek, J. Swaffield, and L. JACK, *Fluid Mechanics*. Pearson Prentice Hall, 2005.
- [2] Fish, Franke E., and Juliann M. Battle. "Hydrodynamic design of the humpback whale flipper" *Journal of Morphology* 225, no. 1 (1995): 51-60.
- [3] Zhang, Mingming, Ming Zhao, and Jianzhong Xu. "Numerical Study of Flow Physics Behind the Aerodynamic Performance on an Airfoil With Leading Edge Tubercles." In *ASME 2016 International Mechanical Engineering Congress and Exposition*, pp. V007T09A085-V007T09A085. American Society of Mechanical Engineers, 2016.
- [4] Xingwei, Zhang, Zhou Chaoying, Zhang Tao, and Ji Wenying. "Numerical study on effect of leading-edge tubercles." *Aircraft Engineering and Aerospace Technology* 85, no. 4 (2013): 247-257.
- [5] Van Nierop, Ernst A., Silas Alben, and Michael P. Brenner. "How bumps on whale flippers delay stall: an aerodynamic model." *Physical review letters* 100, no. 5 (2008): 054502.
- [6] Zain, Nadhirah Mohd, Shabudin Mat, Khushairi Amri Kasim, Shuhaimi Mansor, Md Nizam, and Norazila Othman Dahalan. "Wind tunnel experiments on a generic sharp-edge delta wing UAV Model." *Journal of Advanced Research in Fluid Mechanics and Thermal Science* 40, no. 1 (2017): 18-26.
- [7] Hakim, Muhammad Syahmi Abdul et al., "The effects of Reynolds number on flow separation of Naca Aerofoil," *Journal of Advanced Research in Fluid Mechanics and Thermal Sciences*, Article vol. 47, no. 1, pp. 56-68, 2018.
- [8] Tajuddin, Nurulhuda, Shabudin Mat, Mazuriah Said, and Shumaimi Mansor. "Flow characteristic of blunt-edged delta wing at high angle of attack." *Journal of Advanced Research in Fluid Mechanics and Thermal Sciences* 39 (2017): 17-25.
- [9] Ali, Jaffar Syed Mohamed, and M. Mubin Saleh, "Experimental and numerical study on the aerodynamics and stability characteristics of a canard aircraft," *Journal of Advanced Research in Fluid Mechanics and Thermal Sciences*, Article vol. 53, no. 2, pp. 165-174, 2019.
- [10] Hansen, Kristy L., Richard M. Kelso, and Bassam B. Dally. "Performance variations of leading-edge tubercles for distinct airfoil profiles." *AIAA journal* 49, no. 1 (2011): 185-194.
- [11] Menter, Florian R. "Performance of popular turbulence model for attached and separated adverse pressure gradient flows." *AIAA journal* 30, no. 8 (1992): 2066-2072.
- [12] Gawad, Ahmed Farouk Abdel. "Numerical Simulation Of The Effect Of Leading-Edge Tubercles On The Flow Characteristics Around An Airfoil." In *International Mechanical Engineering Congress & Exposition*. 2012.

- [13] Asli, Majid, Behnam Mashhadi Gholamali, and Abolghasem Mesgarpour Tousi. "Numerical analysis of wind turbine airfoil aerodynamic performance with leading edge bump." *Mathematical Problems in Engineering* 2015 (2015).
- [14] Zhao, Ming, Mingming Zhang, and Jianzhong Xu. "Numerical simulation of flow characteristics behind the aerodynamic performances on an airfoil with leading edge protuberances." *Engineering Applications of Computational Fluid Mechanics* 11, no. 1 (2017): 193-209.
- [15] A. Munshi, E. Sulaiman, N. Omar, and M. Y. Ali, "CFD analysis on the effect of winglet CANT angle on aerodynamics of ONERA M6 wing," *Journal of Advanced Research in Fluid Mechanics and Thermal Sciences*, Journal vol. 45, no. 1, pp. 44-54, 2018.
- [16] McGhee, Robert J., William D. Beasley, and Richard T. Whitcomb. "NASA low-and medium-speed airfoil development." (1979).
- [17] Fish, Frank E., Paul W. Weber, Mark M. Murray, and Laurens E. Howle. "The tubercles on humpback whales' flippers: application of bio-inspired technology." (2011): 203-213.
- [18] F. documentation, "FLUENT 6.3 user's guide," F. Inc, Ed., ed, 2006.
- [19] L. K. Loftin Jr and H. A. Smith, "Aerodynamic Characteristics of 15 NACA Airfoil Sections at Seven Reynolds Numbers from 0.7×10^6 to 9.0×10^6 ," 1949.
- [20] J. M. N. Ashgriz, "An introduction to computational fluid dynamics," in *Fluid Flow Handbook*, J. Saleh, Ed. University of Toronto. Canada: McGraw-Hill Professional 2002, pp. 24.1-24.52.
- [21] P. Spalart and S. Allmaras, "A one-equation turbulence model for aerodynamic flows," in *30th aerospace sciences meeting and exhibit*, 1992, p. 439.